Development of a data-driven framework for monitoring corrosion under droplets

Zhang, Keer; Mol, Arjan; Gonzalez-Garcia, Yaiza

DOI
10.1016/j.corsci.2025.113313

Publication date
2026

Document Version
Final published version

Published in
Corrosion Science

Corrosion Science 258 (2026) 113313

Contents lists available at ScienceDirect

Corrosion Science

journal homepage: www.elsevier.com/locate/corsci

Development of a data-driven framework for monitoring corrosion under droplets

Keer Zhang *, Arjan Mol, Yaiza Gonzalez-Garcia

Delft University of Technology, Department of Materials Science and Engineering, Mekelweg 2, Delft 2628CD, the Netherlands

ARTICLE INFO

Keywords:
Atmospheric corrosion
Corrosion product
Multi-droplet system
Image segmentation
Feature engineering
Data-driven corrosion analysis

ABSTRACT

Understanding localized corrosion under atmospheric droplets is critical, yet previous studies have mostly focused on single-droplet systems or general trends, leaving the role of individual droplets within multi-droplet environments yet to be explored. Here, we present a fully automated, image-based, data-driven framework for analyzing corrosion progression under thousands of droplets simultaneously. Using time-resolved optical imaging and pre-trained large vision models for droplet segmentation, we construct per-droplet color features and propose a probability-based representation of corrosion product formation in inner and outer regions of interest. This approach overcomes the limitations of binary classification by capturing the continuous and spatially heterogeneous nature of corrosion product formation. Applied to carbon steel exposed to over 1500 pre-sprayed 1 M NaCl droplets of various sizes, the method reveals that the probability of corrosion product presence strongly depends on droplet size, with larger droplets more likely to exhibit products both under and around the droplet footprint. Moreover, corrosion products in the outer region can appear independently of under-droplet corrosion, suggesting a role for inter-droplet interactions. By transforming raw imaging data into physically meaningful per-droplet metrics, this work offers a scalable platform for investigating localized corrosion kinetics and morphology in complex, real-world droplet populations, opening new opportunities for connecting droplet formation and population behavior to local and overall atmospheric corrosion rates.

1. Introduction

Droplet-based electrolytes play a crucial role in atmospheric corrosion, especially during its initial stages [1–9]. In multi-droplet systems, electrochemical activity at the solid-liquid interface is influenced not only by droplet size and shape but also by their spatial distribution [10].

Previous studies have primarily focused on single droplets, using electrochemical techniques such as polarization tests [3–5,11], electrochemical impedance spectroscopy (EIS) [3,11], electrochemical noise (EN) [11] analysis, and wire beam electrode (WBE) [1,12] setups to study corrosion kinetics. These experiments often rely on precisely controlled droplet placement, with optical microscopy used to track corrosion product formation over time. For example, Rahimi et al. [11] combined EIS, polarization, and EN with optical imaging for studying corrosion kinetics under a single droplet to examine its link with electrolyte evaporation, droplet geometry, and ion concentration. Analytical models [3,13,14] and finite element modeling (FEM) [14,15] simulations have also been developed to simulate electrolyte spreading, ion transport, and potential fields, although they often rely on assumptions such as fixed droplet shapes, idealized boundary conditions, or steady-state behavior.

Some studies have extended this approach to multi-droplet configurations. Larger droplets have been linked to higher corrosion probability and distinct corrosion types [6,7]. As corrosion progresses, secondary spreading can lead to formation of a thin electrolyte layer surrounding the original droplet footprint [9], which enables inter-droplet interactions that further affect corrosion dynamics. Van den Steen et al. [10] introduced an FEM framework incorporating droplet size distributions and geometries to estimate global corrosion rates. While it accounts for heterogeneity, it assumes steady-state conditions and excludes inter-droplet interactions or time-resolved corrosion product evolution. Other works have combined imaging with kinetic measurements to study corrosion under droplet exposure [2,7,16,17]. For instance, Weissenrieder and Leygraf [7] used QCM and optical microscopy to observe corrosion spreading from a single droplet to adjacent regions. While this study provided valuable mechanistic insight into corrosion spreading dynamics, the analysis was limited to isolated droplet and focused primarily on the propagation event. More

* Corresponding author.
E-mail address: k.zhang-4@tudelft.nl (K. Zhang).

https://doi.org/10.1016/j.corsci.2025.113313
Received 15 May 2025; Received in revised form 8 September 2025; Accepted 9 September 2025
Available online 11 September 2025

recently, Zhang et al. [2] correlated electrical resistance (ER)-based corrosion depth with droplet size distributions as analyzed from in-situ optical imaging. However, this work did not resolve corrosion progression at the individual droplet level.

These studies illustrate the value of image-based analysis in corrosion research and highlight the potential for a method that treats optical microscopy images as a quantitative source. A key step toward this is defining a reliable image-derived indicator that reflects corrosion activity.

Corrosion products offer such an indicator. Their visual appearance, which is usually through color and texture changes, makes them useful for non-invasive tracking into corrosion progression across large droplet populations. In the Evans model, corrosion products accumulate at the droplet center-periphery interface [18]. Other work has shown corrosion products formation both under and outside the droplet [6,7,12]. The distribution and appearance of corrosion products reflect localized electrochemical activity [11,19], making them suitable for kinetic and mechanistic analysis.

To quantify these changes across thousands of droplets, a robust image analysis pipeline is required. This includes:

- Segmentation of individual droplets;
- Extraction of relevant features;
- Numerical and statistical analysis of corrosion patterns.

Traditional segmentation methods (e.g. thresholding [20,21], connected component labeling [2,22]) are being complemented by deep learning techniques [20]. However, such methods often require labeled data and extensive computational effort [23]. More recently, large vision models (LVM), pre-trained across diverse datasets, offer general-purpose segmentation without task-specific training [24].

This work introduces a fully image-based, automated framework for analyzing corrosion under more than 1500 NaCl droplets on carbon steel. Using a pre-trained LVM for segmentation and unsupervised clustering of extracted features, we develop a probability-based representation of corrosion product evolution. This allows continuous tracking of localized corrosion in both inner and outer droplet regions over time.

This work serves two purposes: (1) to demonstrate a scalable, automated approach for quantifying localized corrosion from optical images, and (2) to investigate how droplet size affects corrosion initiation and progression within a multi-droplet environment.

2. Experimental methodology

2.1. Sample preparation and corrosion monitoring

Corrosion experiments were conducted on carbon steel samples under multi-droplet conditions, following the methodology described by Zhang et al. [2]. The focus of the study was on droplet evolution over time; therefore, no kinetic measurements were performed.

Carbon steel specimens (1.5 cm × 1.5 cm, 500 µm thickness) were cut from an EN 10139 DC01-C950 steel sheet using cold cutting. The composition was 0.12 wt% C, 0.6 wt% Mn, 0.05 wt% P, 0.045 wt% S, with Fe as the remainder. Surfaces were mechanically ground using P800 SiC paper to a roughness of 172.68 ± 16.74 nm, measured by atomic force microscopy (AFM, Dimension Edge Scanning Probe Microscope, Bruker Corporation, USA). Samples were then stored in a drying chamber at < 20 % relative humidity for 24 h before exposure.

2.2. Time-lapse imaging

Images were recorded using a Manta G319-C camera (Allied Vision Technologies GmbH, Germany) fitted with a zoom lens (Zoom 1:6.5 W. D.240 mm, Unitron Ltd., USA), mounted above the sample. Illumination was provided by an LED ring light. The zoom was fixed throughout the experiment, giving a field of view of ~11.65 mm × 8.72 mm and capturing ~1600 droplets per frame.

A 1 M NaCl solution was sprayed onto the sample surface to generate droplets, followed by 4 h of free corrosion in a climate chamber. Images were acquired at 2-minute intervals over 3 h and 20 min. A total of 101 frames were selected to represent the corrosion process.

To correct for lighting variation, histogram matching was applied across the image sequence to normalize brightness levels. Minor displacements due to mechanical vibrations were corrected using Fast Fourier Transform (FFT)-based image registration, which aligned all frames to the first frame before further analysis.

3. Results and discussion

3.1. Development of a data-driven framework

To analyze localized corrosion under thousands of droplets, we developed a data-driven framework that tracks visual changes over time. The process consists of three main steps: (1) droplet identification and segmentation using a pre-trained LVM, (2) feature extraction and clustering (3) probability-based modeling of corrosion product evolution.

3.1.1. Droplets segmentation and ROI definition

Each droplet is treated as an individual electrochemical cell that may or may not initiate localized corrosion. To analyze the formation and spread of corrosion products associated with each droplet, two regions of interest (ROIs) are defined: the inner ROI, corresponding to the initial droplet footprint, and the outer ROI, representing a surrounding annular zone with an outer equivalent diameter 9/5 as the inner. This 9/5 ratio is chosen as a conservative boundary based on the physical behavior of the droplets observed in our experiment, as addressed in detail under **S1** in the Supplementary Information. In cases where outer ROIs overlap with the inner ROIs of neighboring droplets, the overlapping areas are excluded from analysis to avoid ambiguity in region attribution (Fig. 1e).

The segmentation process (Fig. 1a-e) begins with the first image in the time-lapse sequence. A pre-trained vision model, Segment Anything Model (SAM) [25], identifies individual droplets from the background. As SAM occasionally merges adjacent droplets (Fig. 1f), we filter masks based on spatial overlap and convert the remaining masks into binary format (Fig. 1b). Connected component labeling assigns unique identifiers to each droplet (Fig. 1c-d), which are then tracked throughout the sequence using brightness-normalized and spatially aligned frames. Outer ROI are generated via morphological dilation (Fig. 1e).

3.1.2. Feature extraction and clustering

The color and spatial distribution of corrosion products serve as important indicators of the underlying corrosion process. These visual features can provide insight into the severity of corrosion and the possible composition of the corrosion products [11]. The darkening observed is a well-known characteristic of the formation of iron oxide/hydroxide layers on steel, which have low optical reflectivity. To directly validate that this optical darkening corresponds to corrosion in our experiments, post-mortem SEM-EDS analysis is performed on a representative sample (see section **S2** in the Supplementary Information), which confirms that the dark regions are composed of iron- and oxygen-rich corrosion products.

To track these changes, each ROI is first interpolated to a fixed size of 32 × 32 pixels using a high-quality bicubic interpolation (cv2.INTER_CUBIC) to preserve feature integrity and masked to exclude non-droplet regions (Fig. 2a). Three feature engineering strategies are then applied to extract color information from the inner and outer ROIs: (1) radial segmentation, where pixels are grouped by angular sectors (Fig. 2b); (2) concentric segmentation, where pixels are grouped based on radial distance from the droplet center (Fig. 2c); and (3) autoencoder-based encoding [26,27], where unsupervised neural networks are trained

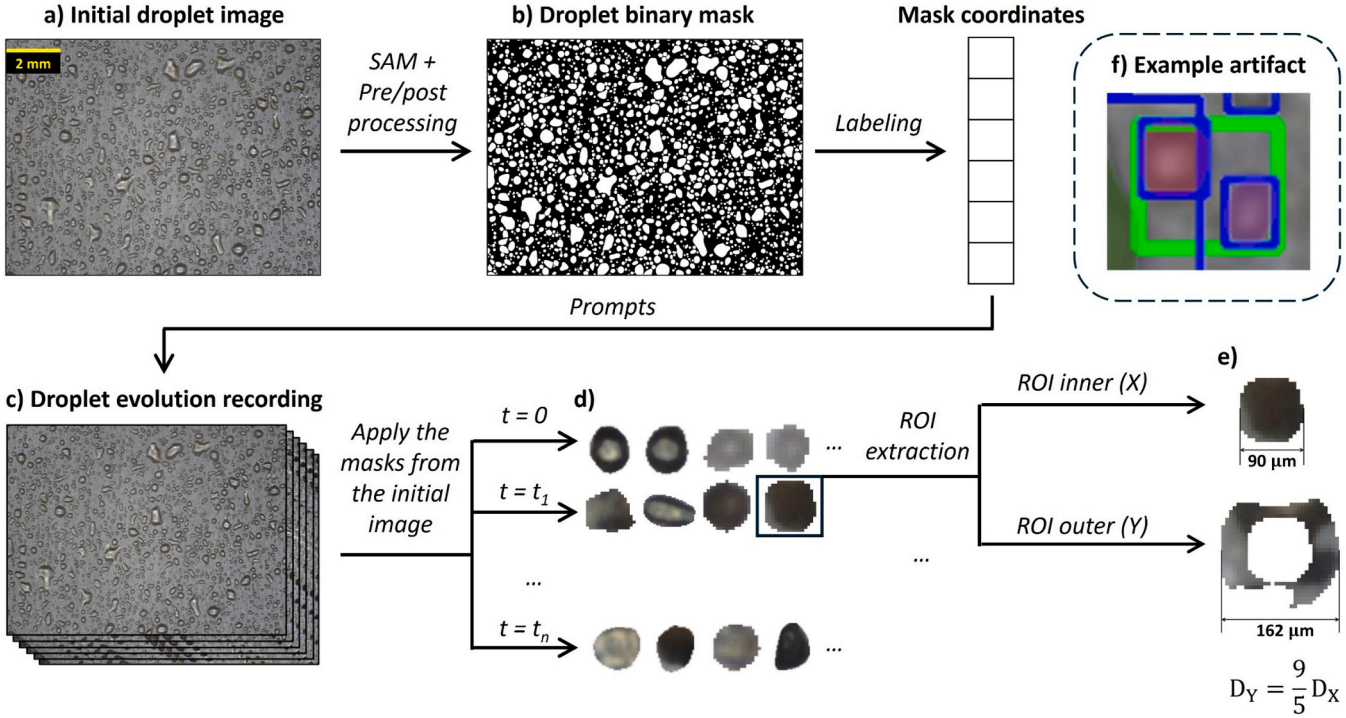

Fig. 1. ROI extraction workflow for droplet-induced corrosion analysis: (a) Initial droplet image used for segmentation (b) Binary mask of droplet locations after post-processing (c) Time-lapse tracking of droplet-covered areas (d) Tracked droplet segments at selected exposure times (e) Inner and outer ROIs for a representative droplet, with overlapping regions excluded (f) Segmentation artifacts in SAM output, where adjacent droplets are merged.

separately for inner and outer ROIs (Fig. 2d). The feature engineering strategies are chosen to capture key physical characteristics of corrosion patterns. The concentric segmentation method aligns with the classic Evans droplet model, which describes distinct, concentric anodic and cathodic zones due to the oxygen gradient along droplet radius. The radial segmentation method emphasizes the asymmetrical nature of real-world corrosion where corrosion usually initializes at localized defects. Autoencoder is included as a data-driven approach to learn more complex spatial patterns without domain-specific assumptions.

For radial/concentric methods, we compute the mean and variance of RGB channels per subgroup. To account for the observation that corrosion products within an outer ROI are often unevenly distributed [12], which typically appears in localized areas rather than forming a uniform ring around the droplet, we also extract grayscale gradient featured for the outer ROIs: (1) the mean and variance of all pairwise pixel intensity differences, which capture the overall variation and contrast within the region; and (2) a normalized intensity histogram computed over 5 bins spanning the full grayscale range [0, 255] which provides a coarse representation of the pixel intensity distribution.

The total number of features for the segmentation-based methods therefore scales with the number of segments chosen. For the autoencoder method, two autoencoders are trained separately on inner and outer ROIs to extract the same number of features from each ROI. A detailed description of the procedures can be found in **S3** under the Supplementary Information.

Based on a multi-stage optimization process, the concentric segmentation method is selected for final analysis. A subsequent grid search evaluated by the Silhouette score determines that the ideal parameters are 5 segments for the inner ROIs and 2 for the outer ROIs. The final number of Principal Components (PCs) is determined to be 5 for both regions to retain over 90 % of the variance from the complete dataset. The detailed methodology for the entire selection and optimization process is provided in **S4** under the Supplementary Information.

K-means++ clustering groups ROIs into corrosion and non-corrosion types. The results (Fig. 3a-b) show clear separation, the choice of 2 clusters is determined to be optimal as it yields the highest Silhouette score for both regions (see Figure S5 in Supplementary Information **S4**). The resulting Silhouette scores of 0.72 for inner ROIs and 0.53 for outer ROIs validate the clustering quality.

Mapping the reduced feature space back to the original ROIs reveals that one cluster (green) is associated with a strong presence of corrosion products, whereas the other (blue) corresponds to droplets with minimal or no corrosion.

3.1.3. *Continuous probability-based mapping of corrosion evolution*

While clustering captures final corrosion status, it does not reflect when corrosion begins or how it progresses. One potential approach to extract this kinetic information is to perform clustering on the time series of each droplet's ROI and assign a binary transition label from "no corrosion" to "corrosion". However, this approach oversimplifies the process and is inadequate for capturing the gradual, heterogeneous evolution observed in practice (see **S5** under Supplementary Information).

To address this, we convert PCA-reduced features into continuous probability curve for each ROI over time. As illustrated in Fig. 4, the K-Means++ classifier effectively separates the ROIs into distinct clusters but treats all samples within a cluster equally, disregarding variations within each group. To overcome this limitation, we replace the discrete cluster labels with a probability distribution that reflects the likelihood of each sample belonging to the identified clusters.

$$\sigma_1(A) = \frac{e^{-d(A,C_1)}}{e^{-d(A,C_1)} + e^{-d(A,C_2)}}$$
$$\sigma_2(A) = \frac{e^{-d(A,C_2)}}{e^{-d(A,C_1)} + e^{-d(A,C_2)}} \quad (1)$$
$$with\ \ d(A,C_a) = \sqrt{\sum_{i=1}^{n} w_i (A_i - C_{a,i})^2} \quad \forall a \in \{1,2\}$$

This probabilistic approach is based on the weighted distances

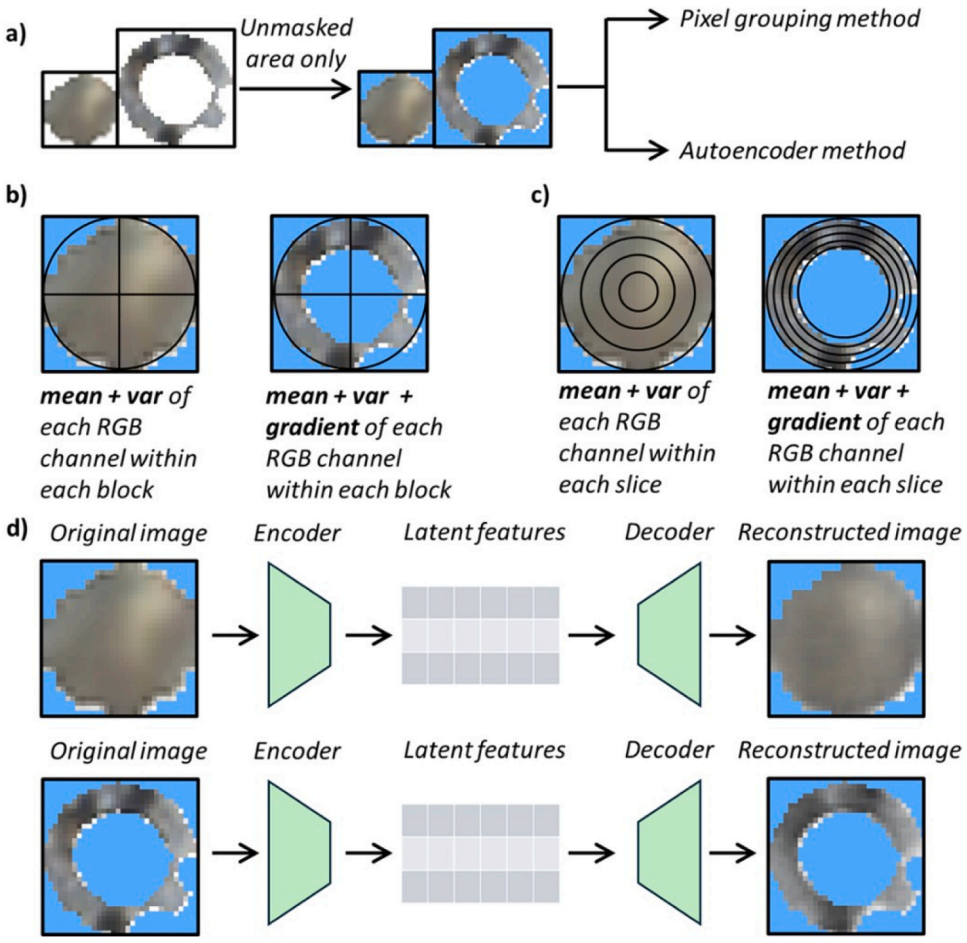

Fig. 2. Feature engineering strategies for ROI analysis, using the final image in the time-lapse sequence. All ROIs are resized to 32 × 32 pixels. Only droplet-covered (unmasked) regions are included. (a) ROI masking to remove background pixels. (b) Radial segmentation of pixels by angular sector. (c) Concentric segmentation of pixels by radial distance. Regarding b and c, for illustration, each ROI is divided into four subgroups. (d) Autoencoder-based feature extraction trained separately for inner and outer ROIs.

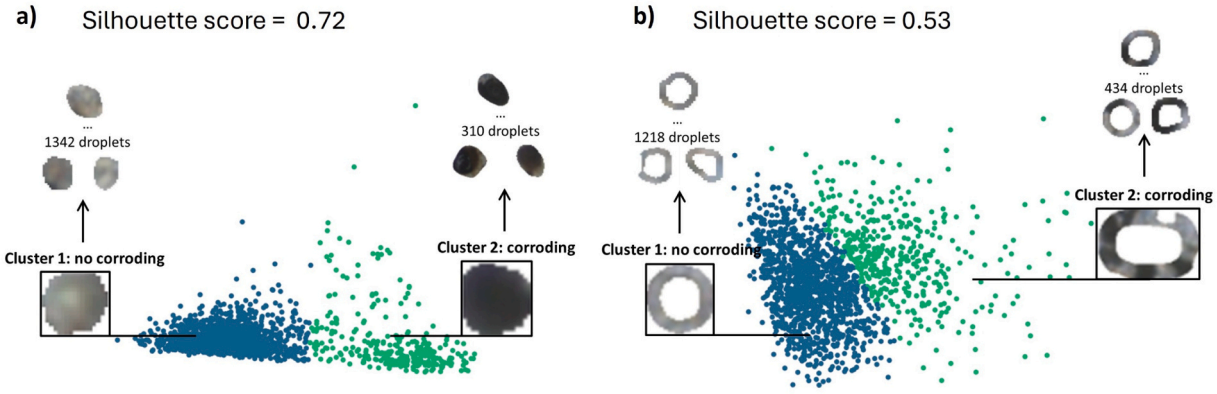

Fig. 3. K-means++ clustering of PCA-reduced features for **(a)** inner ROIs and **(b)** outer ROIs. The plot is shown in space defined by the first two PCs for illustrative purposes. Cluster separation corresponds to corrosion vs. non-corrosion categories, normalized using MaxAbs (inner) or MinMax (outer) scaling.

between a sample and each cluster center. As shown in Eq. (1), the distances to the centers of the blue and green clusters, denoted as $d(A, C_1)$ and $d(A, C_2)$ are calculated using weights representing the normalized explained variance ratio obtained during PCA. A negative sign is applied to reflect the inverse relationship between distance and cluster membership probability.

A SoftMax operation is then applied to convert these opposite distances into probabilities: $\sigma_1(A)$ and $\sigma_2(A)$, representing the likelihood of A belonging to the blue or green cluster, respectively. This transformation ensures that the two probabilities sum to 1 and amplifies the contrast between samples when one cluster is clearly more likely than the other.

By extending the method to the entire droplet recording, for each droplet, we obtain a time series of probabilities:

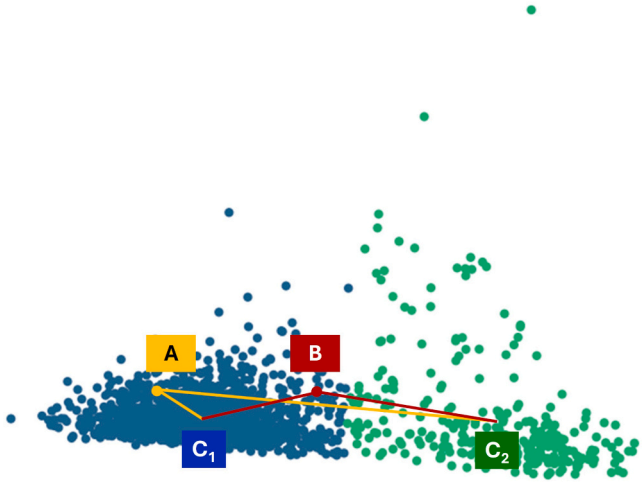

Fig. 4. Probability-based representation of corrosion status for two inner ROI data points (A and B), based on weighted distance to cluster centers (C1 and C2) in PCA space. Colors match cluster assignments in Fig. 3.

- $p_{X,t}$: the likelihood of corrosion product in the inner ROI at time t
- $p_{Y,t}$: same for the outer ROI

The validity of using end-frame cluster centers to analyze the entire time series is confirmed with a consistency check, which is detailed in **S6** under the Supplementary Information. This yields a smooth temporal profile of corrosion product evolution (Fig. 5) which enables detailed analysis of initiation, progression, and stabilization on a per-droplet basis.

3.2. Application of the framework

With the framework, covering segmentation, feature extraction, unsupervised clustering, and probability-based tracking, in place, we now apply it to analyze the spatiotemporal behavior of corrosion across a large droplet population. We first examine representative cases, then assess population-wide corrosion kinetics, and finally investigate how droplet size influences both corrosion type and evolution.

3.2.1. Representative corrosion behaviors

To illustrate typical corrosion patterns, we begin with two droplets categorized as corroding or non-corroding based on the clustering results from the final image (Section 3.1.2). Fig. 5 shows their probability curve (a-b: corroding, c-d: non-corroding) over time, as derived from the framework introduced in Section 3.1.3. In Fig. 5a, the inner ROI probability p_X (light blue solid curve) rises gradually and stabilizes near 1.0 by 50 min, indicating substantial accumulation of corrosion products. A Savitzky-Golay filter [28,29] is applied to extract the general trend from the original data. The smoothed trend (orange curve) is consistent with image darkening over time and highlights three key kinetic features: transition onset (vertical dark blue dashed line), plateau start (vertical yellow dashed line), and midpoint between them (vertical red dashed line). From these points, we extract key kinetic descriptors: the transition interval is the duration between the onset and the start of the plateau. The transition slope is defined as the average rate of change of the probability during this interval, calculated from the smoothed curve. A steeper slope indicates a more rapid stabilization of corrosion products accumulation. Once the plateau is reached, no significant visual changes are observed, which aligns with the stabilization of p_X.

Fig. 5**b** shows the corresponding outer ROI probability p_Y, which also increases and stabilizes around 0.8, confirming corrosion product accumulation beyond the droplet footprint. This is further supported by the corresponding image sequences showing the evolution around the droplet periphery.

A comparative analysis of Figs. 5a and b indicates that corrosion product formation begins earlier in the inner ROI than in the outer ROI. This observation aligns with the findings of Wang et al. [12], who reported that while pitting and uniform corrosion tend to occur within or near the droplet periphery, while minor corrosion processes may develop outside the droplet over time.

In contrast, Figs. 5**c** and **d** depict a droplet where no significant corrosion product formation occurs. In Fig. 5**c**, p_X curve initially rises to approximately 0.4, then declines to near zero after 100 min. Image inspection suggests that this behavior can be related to the droplet drying process. In our previous work [2], we have shown that certain contact angles can lead to optical effects such as ring-shaped illumination or reflection/refraction patterns that darken the droplet edge. Although these effects are not distinctly observable here due to resolution limits, the early dark rim is evident and fades over time as the droplet dries and the contact angle decreases. The p_Y curve (Fig. 5**d**) remains consistently low, fluctuating range between 0.0 and around 0.1, which confirms the absence of corrosion product formation in the outer ROI of this droplet.

These representative cases illustrate the outcomes where either both ROIs show significant accumulation or neither does. Apart from that, our framework also quantitatively describes other distinct corrosion patterns reported in the literature. For example, Soulie et al. [30] observed that corrosion products under a 1 M NaCl droplet is predominantly confined within the droplet footprint. This corresponds to a high p_X plateau and low p_Y in our representation. Conversely, Weissenrieder et al. [7] described corrosion that initiates at the periphery of the droplet and propagates outward, forming filiform-like corrosion morphology. Risteen et al. [6] further demonstrated that such behavior is strongly influenced by droplet size. Within our framework, this would manifest as a high final p_Y plateau and a low p_X.

While clustering on the end-of-exposure image (Section 3.1.2) provides an initial corrosion/non-corrosion categorization, a more physically meaningful definition based on the full time-resolved probability curves will be adopted in the following analysis, where ROI corrosion status is determined based on their long-term behavior. An ROI is considered "corroding" if its probability curve (p_X or p_Y) shows a sustained transition and stabilizes at a high plateau ($p > 0.5$) which indicates a sustained existence of corrosion products. Conversely, a "non-corroding" ROI is one where the probability remains low. The robustness of the choice regarding the probability threshold and plateau duration for end-stage plateau detection is demonstrated by a sensitivity analysis in the Supplementary Information under **S7**.

3.2.2. Comparative temporal analysis of corrosion progression in inner and outer ROIs

The data-driven framework allows a direct comparison of corrosion kinetics (i.e. transition midpoint, transition intervals, and transition slopes) between inner (X) and outer (Y) ROIs. We focus on ROIs that develop a clear, sustained presence of corrosion products, defined by the probability curve stabilizing at a plateau over 0.5.

Fig. 6 show that corrosion products on average appear earlier and accumulate faster in inner ROIs. This observation is consistent with individual cases discussed in Section 3.2.1. In Fig. 6**a,** the histogram of transition midpoints shows that the kernel density estimation (KDE) for p_X peaks earlier than for p_Y, indicating faster initiation in the inner region. Fig. 6**b** shows that the transition intervals (onset to plateau) are also shorter for p_X, suggesting a faster corrosion stabilization. This is further supported by Fig. 6**c**, where the KDE of transition slopes is steeper for p_X, confirming faster corrosion product accumulation in the inner region.

Fig. 7**a** compares two representations of corrosion product occurrence over time: the "soft representation", based on average probability values (solid curves), and the "hard representation", based on the binary classification of whether $p > 0.5$ at each time step. Fig. 7**a** also suggests that another contributing factor of p_X peaks at a higher value than p_Y in

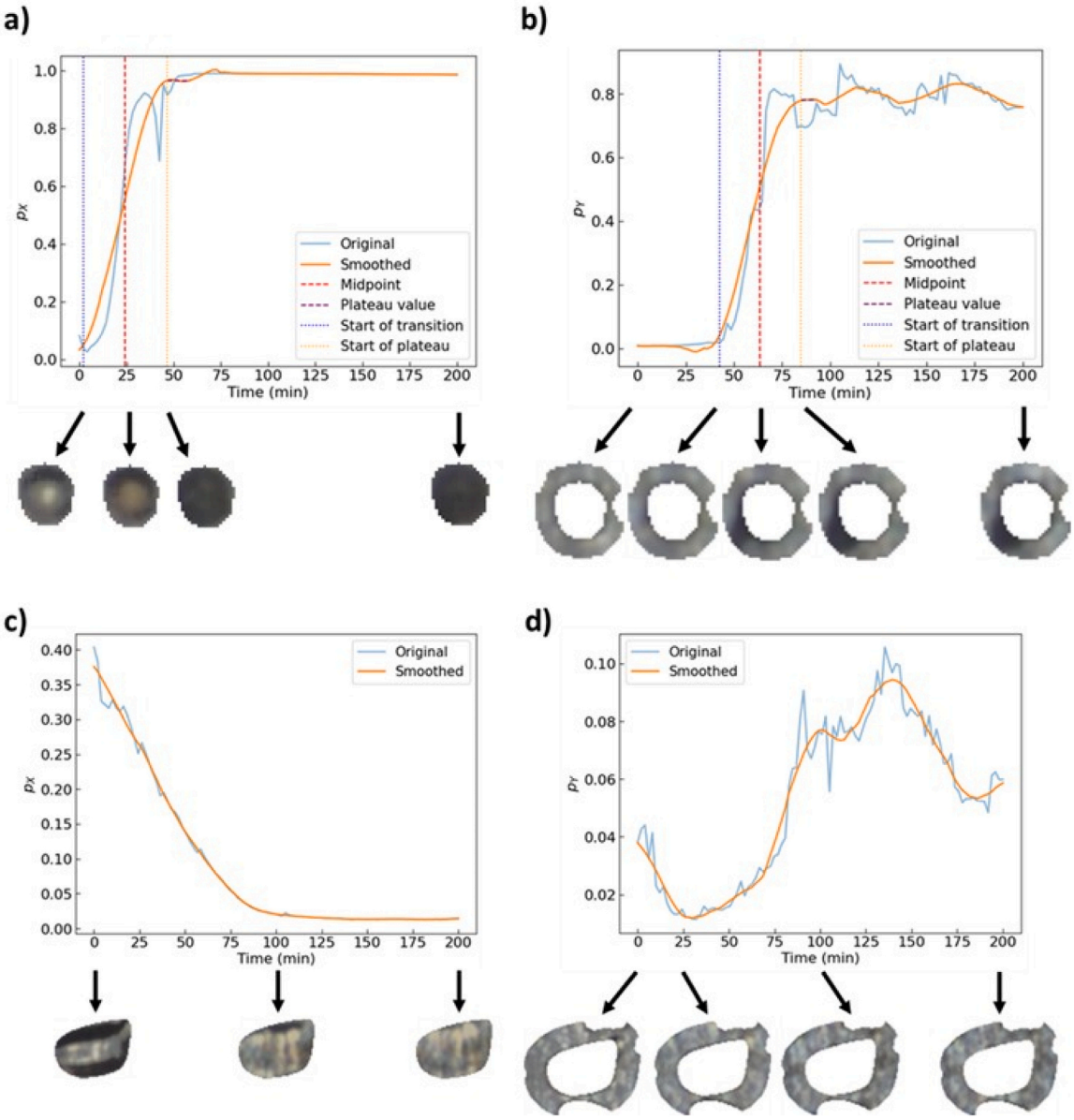

Fig. 5. Representative corrosion probability curves and corresponding ROI images. **(a)** Inner ROI (p_X) for a corroding droplet, with raw (blue) and smoothed (orange) curves, and marked onset, midpoint, and plateau. **(b)** Outer ROI (p_Y) for the same droplet. **(c)** Inner ROI probability for a non-corroding droplet. **(d)** Outer ROI probability for the same non-corroding droplet.

Fig. 6**c** might be explained by the generally high values of p_X compared to p_Y. This is also theoretically valid, as corrosion product coverage is often more substantial in the inner ROI, making it more likely to exhibit either a strong presence or complete absence of corrosion products which leads to more extreme higher p_X values.

The "soft" and "hard" representation can be described with Eqs. (2) and (3):

$$\overline{p_a^t} = \frac{1}{N_a}\sum_{i=1}^{N_a} p_{i,a}^t \text{ where } N_a = \#\left(a^{end} = 1\right) \forall a \in \{X, Y\} \tag{2}$$

$$Frac_a^t = \frac{1}{N_a}\sum_{i=1}^{N_a} 1\left(p_{i,a}^t > 0.5\right) = \frac{n_a^t}{N_a} \text{ where } n_a^t = \#(a^t = 1) \forall a \in \{X, Y\} \tag{3}$$

where N_a denotes the number of droplets containing corrosion products in the inner or outer ROI at the final stage, while $p_{i,a}^t$ represents the dynamic probability of corrosion product existing in the inner or outer ROI of droplet i at time t, and n_a^t stands for the number of droplets containing corrosion products in the inner or outer ROI at time t. $a^t = 1$ and $a^{end} = 1$ explicitly mean inner ($a = X$) or outer ($a = Y$) ROI shows presence of corrosion product at time t and by the end of exposure.

The close match between the two, as shown in Fig. 7**a**, confirms that the probability-based representation provides a soft yet accurate approximation of the corrosion fraction. The two curves follow a similar overall trend, with the probability-based curve initially being slightly higher and later slightly lower than the fraction-based curve. This behavior reflects the nature of the probability assignment: droplets located near cluster boundaries in feature space receive intermediate probability values rather than discrete 0 or 1 labels. As a result, the probability-based representation exhibits a smaller dynamic range compared to the binary count, while preserving the overall shape of corrosion evolution. Importantly, although the global averages are similar, the "soft representation" offers finer-grained, per-droplet information, which captures gradual corrosion transitions that would be lost under "hard representation". This relationship is further supported

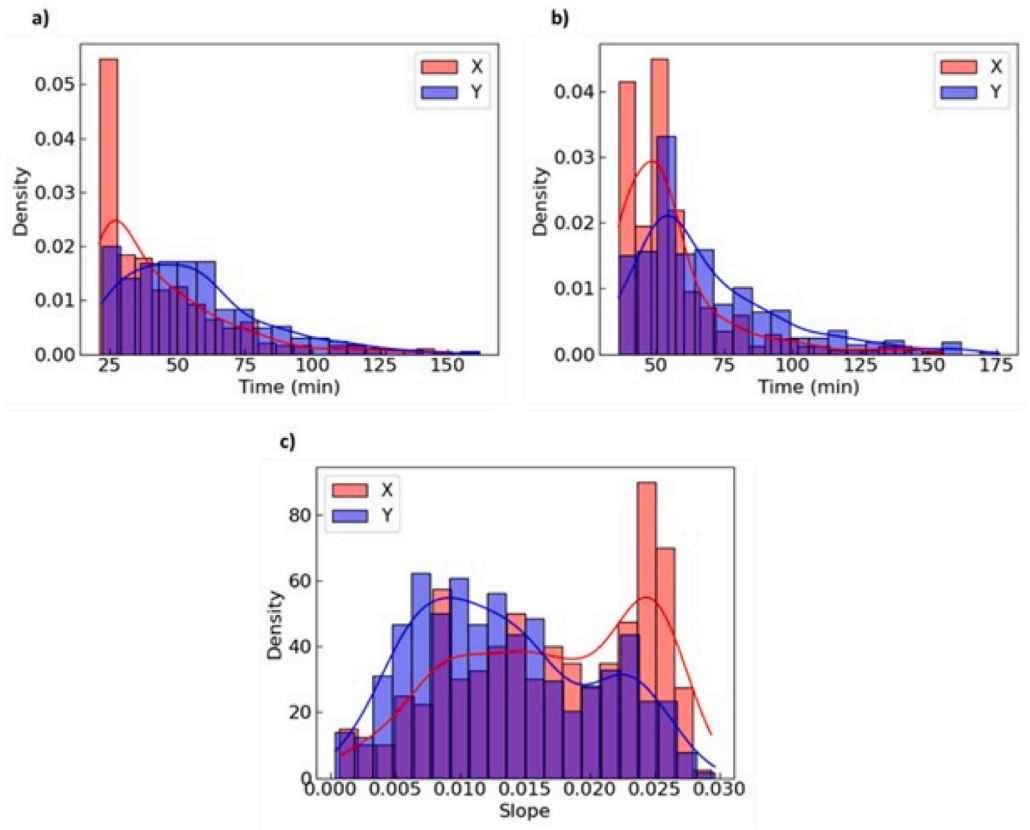

Fig. 6. Statistical comparison of corrosion kinetics between inner (red) and outer (blue) ROIs for droplets classified as corroding at the end of the exposure. **(a)** Transition midpoint. **(b)** Transition intervals (onset to plateau). **(c)** Transition slopes.

by Fig. 7**b**, which shows a mostly linear correlation between the two representations over time, validating Eq. (4):

$$\frac{n_a^t}{N_a} = \alpha_a \bullet \overline{p_a^t} + \beta_a \; \forall a \in \{X, Y, XY\} \tag{4}$$

Eq. (4) can be further extended to droplets that show corrosion products at both inner and outer ROIs at the end of exposure, as validated by Fig. 7**c**. To explore the interaction between inner and outer ROIs, we focus on droplets that have already developed corrosion in one region at certain time and investigate the fraction that simultaneously exhibit corrosion in both regions ($\frac{n_{XY}^t}{n_X^t}$ or $\frac{n_{XY}^t}{n_Y^t}$). Within the "soft representation", the joint probability of corrosion in both ROIs ($p_{i,XY}^t$) is approximated as the product of the individual probabilities ($p_{i,X}^t$ and $p_{i,Y}^t$) since they are separately analyzed and therefore statistically independent. Eq. (5) shows the correlation between the "soft" and "hard" representations by applying Eq. (4) to three groups of droplets: those showing corrosion in the inner ROI ($a = X$), the outer ROI ($a = Y$), and both ROIs ($a = XY$) at end of exposure.

$$\frac{n_{XY}^t}{n_a^t} = k_a \bullet \frac{n_{XY}^t}{N_{XY}} \bullet \frac{N_a}{n_a^t} = k_a \bullet \left(\alpha_{XY} \bullet \overline{p_{XY}^t} + \beta_{XY}\right) \Big/ \left(\alpha_a \bullet \overline{p_a^t} + \beta_a\right) \approx k_a \bullet \overline{p_{XY}^t} \Big/ \overline{p_a^t}$$

$$\text{where } k_a = \frac{N_{XY}}{N_a} \; \forall a \in \{X, \; Y\}$$

$$\text{and } p_{i,XY}^t = p_{i,X}^t \bullet p_{i,Y}^t \; \forall i \in \{1, \ldots, N_{XY}\} \tag{5}$$

Fig. 7**d** presents the evolution of co-corrosion for inner and outer ROIs. The red curves, representing the co-development analysis regarding inner ROIs, stabilize above 0.6. This indicates that the majority of those droplets showing corrosion products at inner ROI also develop corrosion products at their outer ROI. This observation supports earlier findings by Wang et al. [12], suggesting that under-droplet corrosion often propagates outward due to electrochemical or diffusional effects.

In contrast, the blue curves show that only 40 % of the droplets exhibiting corrosion in the outer ROI also show corrosion in the inner ROI. This suggests that outer-region corrosion may occur independently of corrosion under the main droplet footprint. One hypothesis is that this is potentially due to inter-droplet interactions or diffusion of chemical species between neighboring droplets. A target analysis shows that the droplet spatially clustering behavior can both slightly increase the overall probability and accelerate the onset of outer ROI corrosion, as detailed under **S8** in the Supplementary Information. Another explanation is that these independent outer corrosion events are governed by other factors such as corrosion initiating at the three-phase boundary of a single droplet and subsequently propagating outward, as previously observed by Risteen et al. [6] and Weissenrieder et al. [7]

In summary, the comparative temporal analysis reveals distinct kinetic profiles and propagation pathways for the inner and outer ROIs. The statistical analysis of the kinetic descriptors demonstrates that corrosion product formation initiates earlier and stabilizes more rapidly in the inner region. Furthermore, the analysis of co-development fractions shows an asymmetric relationship: while under-droplet corrosion has a high probability of propagating outward, a significant portion of outer-region corrosion occurs independently. These findings suggest a primary "inner-to-outer" corrosion mechanism, supplemented by an independent initiation process at the droplet periphery.

3.2.3. Influence of droplet size on corrosion probability

With the corrosion behaviors classified in a scale-invariant manner, the influence of the original, physical droplet size can now be systematically investigated. Droplet size plays a critical role in determining droplet-induced corrosion by influencing not only the likelihood of

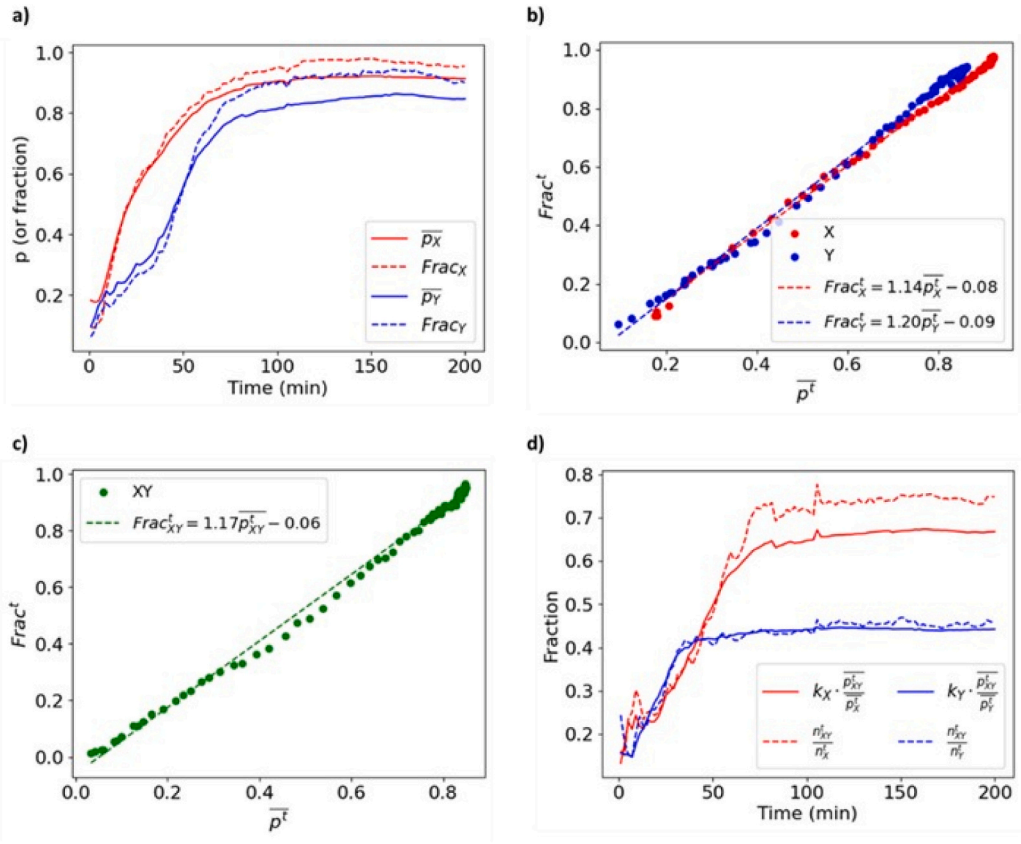

Fig. 7. Comparison of "soft" (probability-based, solid lines) and "hard" (binary classification, dashed lines) corrosion representations. **(a)** Temporal evolution of average corrosion status for inner (red) and outer (blue) ROIs. **(b)** Correlation between soft and hard representations for droplets showing corrosion product at inner (red) and outer (blue) ROIs at the end of exposure. **(c)** Correlation between the two representations for droplets showing corrosion product at both inner and outer ROIs at the end of exposure **(d)** Co-development of corrosion in both ROIs, expressed for droplets corroding in the inner (red) or outer (blue) ROI.

corrosion the occurrence but also the type and rate of corrosion progression [4,6,18,31]. A previous study [6] has shown that for carbon steel, the probability of Evans-type corrosion increases with droplet size, with a threshold beyond which nearly all droplets exhibit this corrosion mode.

In the context of the present study, this behavior corresponds to p_X stabilizing at a high plateau, regardless of the evolution of p_Y. Conversely, corrosion products that primarily from outside the droplet footprint, represented by p_Y stabilizing at a high plateau while p_X remains low, are more frequently associated with smaller droplets. This trend is evident in Fig. 8.

Fig. 8a presents the distribution of droplets across size bins, along with the fraction exhibiting corrosion at either the inner or outer ROIs by the end of exposure. The size bins are defined as uneven ranges to avoid excessively low droplet counts in the larger size categories. A monotonic increase in corrosion fraction can be observed with increasing droplet diameter for both inner and outer ROIs. While smaller droplets dominate the population, density-normalized histograms (Fig. 8b) and cumulative density functions (Fig. 8c) confirm that this trend is not an artifact of population imbalance. Specifically, in Fig. 8**b**, the KDE curves for droplets classified as $X_{end} = 0$ or $Y_{end} = 0$ peak at much smaller value than that for either $X_{end} = 1$ or $Y_{end} = 1$. The cumulative distribution curves in Fig. 8**c** further support this trend: droplets without corrosion products in the inner or outer ROI reach a plateau at lower diameters compared to those with corrosion ($X_{end} = 1$ or $Y_{end} = 1$).

The finding that the probability of developing optically detectable corrosion increases with droplet size is a real physical phenomenon and not simply an artifact of optical detection limits. This trend is consistent with the previous study [6] that uses direct profilometry to measure metal volume loss, where the trend that the fraction of drops showing corrosion increases with drop size is also observed. This confirms that while trace electrochemical activity might exist, the likelihood of significant and visible corrosion initiation is strongly size-dependent.

Comparing corrosion development in the inner versus outer ROIs, it is observed that the presence of corrosion products in the inner ROI is more strongly associated with larger droplet sizes. As shown in Fig. 8**a**, the fraction of droplets exhibiting corrosion at the inner ROI increases more steeply with droplet size compared to the outer ROI. In contrast, droplets exhibiting corrosion at the outer ROI appear across a broader size range, maintaining a relatively higher fraction even at intermediate droplet sizes (Fig. 8**a**). This observation is further supported by the density-normalized size distributions (Fig. 8**b**) and cumulative density functions (Fig. 8**c**), where droplets with inner ROI corrosion ($X_{end} = 1$) are shifted toward larger diameters relative to those with outer ROI corrosion ($Y_{end} = 1$), which suggests that corrosion at the outer ROI may be less dependent on individual droplet size and more influenced by inter-droplet interactions or diffusional processes.

In Fig. 8**d-f**, the droplet behavior based on ROI is categorized into three types: non-corroding ($X_{end} = 0$ and $Y_{end} = 0$), Evans-like corrosion ($X_{end} = 1$, no matter of Y), and corrosion localized outside the droplet footprint ($X_{end} = 0$ and $Y_{end} = 1$), based on the previous investigation [6]. Overall, the probability of a droplet undergoing corrosion increases with its size, with Evans-type corrosion becoming dominant beyond a critical droplet diameter. Corrosion localized only in the outer ROI may be due to inter-droplet effects or diffusion of corrosion products from neighboring droplets. This phenomenon is more frequently observed in droplets of intermediate size. As presented Fig. 8**f**, when the droplet diameter exceeds approximately 360 μm, nearly all droplets exhibit signs of corrosion, and above 650 μm, all corrosion predominantly follows the Evans-like pattern.

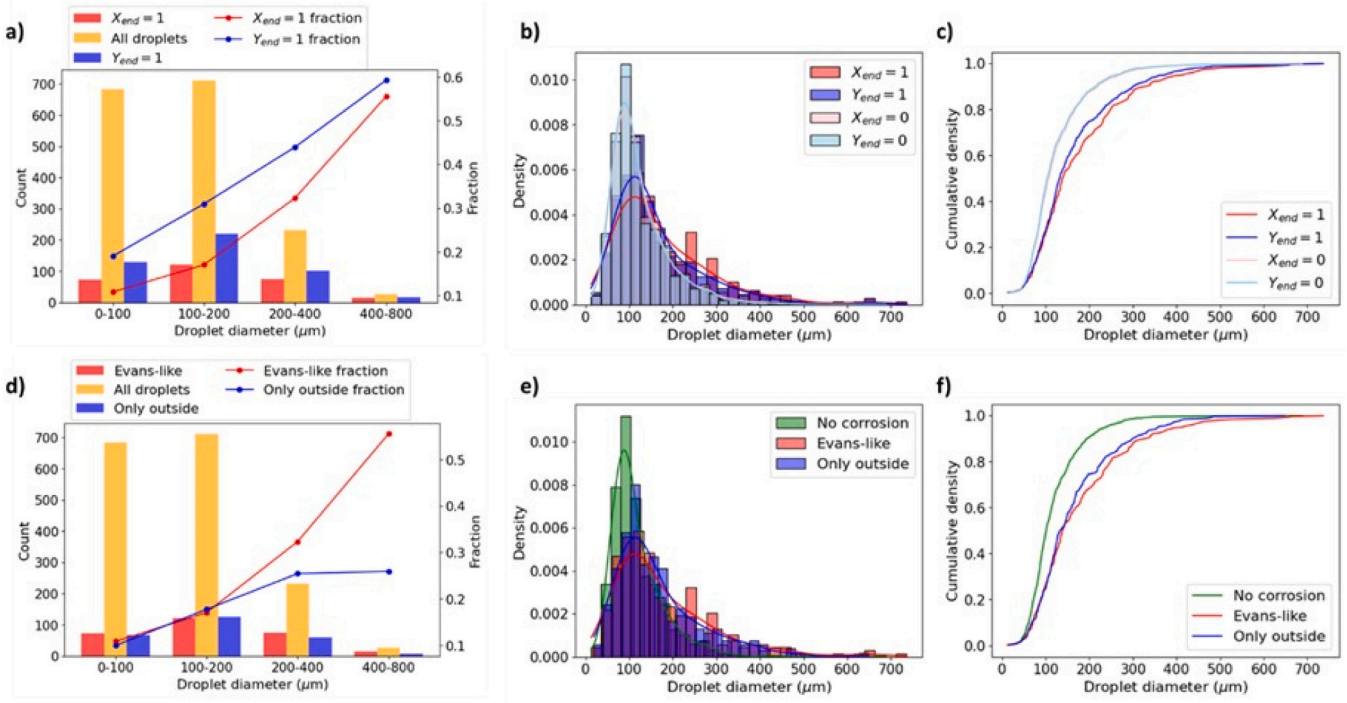

Fig. 8. Influence of droplet size on corrosion probability and type. (a) Droplet counts (bars) and corrosion fractions (lines) by size bin for inner (red) and outer (blue) ROIs. (b) Normalized size distributions for corroding vs. non-corroding droplets in each ROI. (c) Cumulative distributions of droplet size for the same categories in (b). (d) Fractions of Evans-like (red) and outer-only (blue) corrosion types by size bin. (e) Normalized size distributions for non-corroding (green), Evans-like (red), and outer-only (blue) corrosion types. (f) Corresponding cumulative distributions shown in (e).

These observations confirm that droplet size is a critical factor governing both the likelihood and the dominant mode of corrosion, with larger droplets favoring under-droplet (Evans-like) corrosion, while intermediate-sized droplets may promote corrosion in surrounding regions due to inter-droplet interactions or product diffusion.

3.2.4. *Influence of droplet size on corrosion characteristics over time*

The previous section focused on the influence of droplet size on whether corrosion occurs and type of corrosion by the end of the exposure, while droplet size also has a significant impact on corrosion kinetics. Jiang et al. [3] have reported that the cathodic limiting current

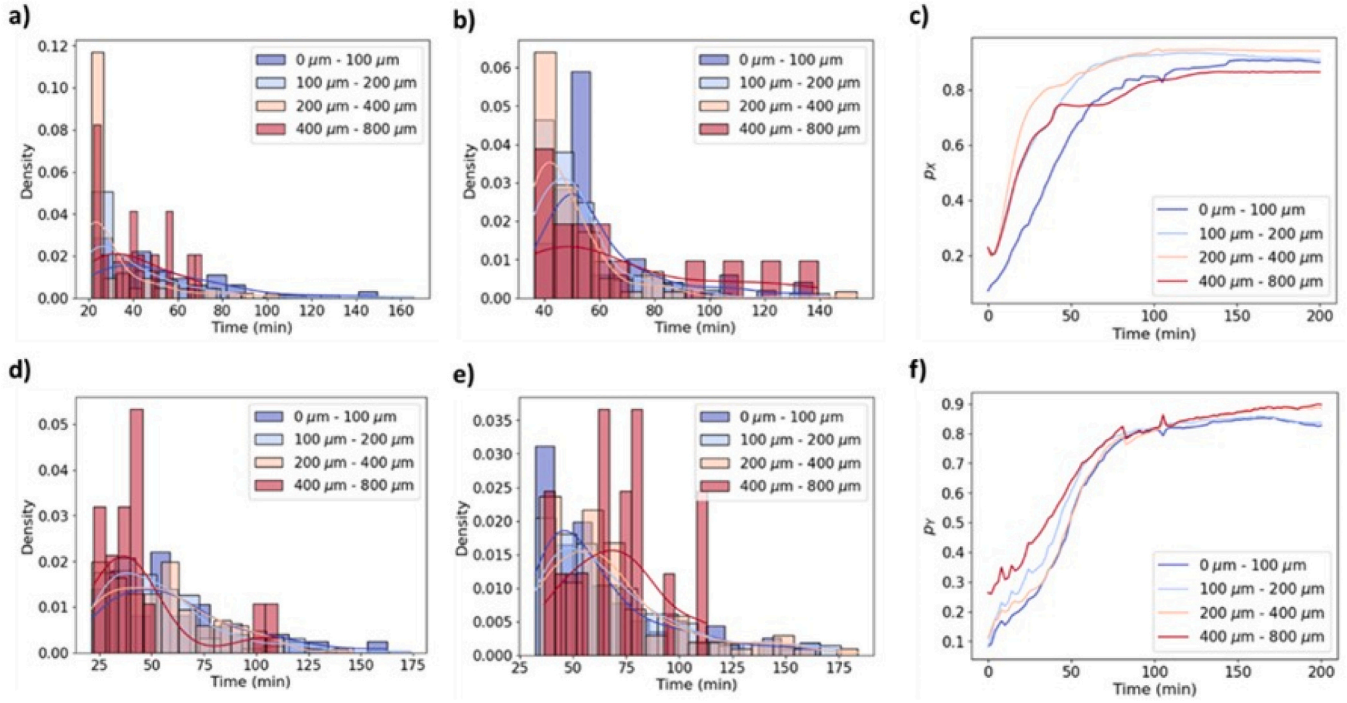

Fig. 9. Effect of droplet size on corrosion kinetics. (a-b) Transition midpoints and intervals for inner ROIs. (c) Average p_X evolution for droplets of different sizes. Only inner ROIs with corrosion product presence at the end of exposure are included in (a)-(c). (d-e) Transition midpoints intervals for outer ROIs. (f) Average p_Y evolution for droplets with different sizes. Only outer ROIs with corrosion products presence at the end of exposure are included (d)-(f).

increases linearly with the inverse of droplet radius, indicating that corrosion under larger droplets might be constrained by oxygen concentration at the solid-liquid interface. Cole et al. [14] have further showed that larger droplets exhibit a more pronounced oxygen concentration gradient along the radius, favoring cathodic reactions near the droplet edge. In addition, as droplets evaporate, their initial size influences the drying rate and thus the evolution of electrolyte concentration. Lequien et al. [32] have demonstrated that even within a single droplet, local concentration gradients might emerge due to enhanced vapor flux at the edges, which induces diffusion, capillary flow, and Marangoni flow, all strongly dependent on droplet size. Furthermore, the transport and precipitation of corrosion products, both inside and outside the droplet, are also affected by droplet dimensions [18].

In this section, we analyze the influence of droplet size on two temporal descriptors: the transition midpoint, indicating when corrosion products begin to appear, and the transition interval, reflecting how fast corrosion product accumulation stabilizes. The metrics are evaluated separately for the inner and outer ROIs to extend the previous global analysis into a size-dependent context. For consistency, droplet diameters are classified into the same ranges as presented in Fig. 8.

Fig. 9 presents normalized histograms of these characteristics across droplet size bins. In the inner ROIs, Fig. 9a shows that droplets of intermediate size (100 μm to 400 μm) tend to reach the transition midpoint slightly earlier than smaller (0 μm to 100 μm) or larger (400 μm to 800 μm) droplets. Similarly, Fig. 9b reveals that these intermediate-sized droplets also exhibit slightly shorter transition intervals, suggesting faster stabilization of corrosion product accumulation. This behavior may result from an optimal balance between oxygen solubility and ionic conductivity. Larger droplets tend to retain volume longer and maintain lower chloride concentration, enhancing oxygen solubility but reducing electrolyte conductivity. Fig. 9c shows the average evolution of p_X for droplets of different sizes. Larger droplets tend to stabilize at a lower plateau value, possibly due to less uniform corrosion product precipitation across the initial footprint.

For outer ROIs, the trend differs. Fig. 9d-e show that larger droplets (400 μm to 800 μm) initiate corrosion earlier, while smaller ones (0 μm to 100 μm) stabilizes more quickly. Earlier appearance of corrosion products in larger droplets can be attributed to enhanced evaporation at droplet edges, which results in a higher chloride concentration and thereby creating a more aggressive environment that promotes early corrosion initiation at the periphery. In contrast, the fast drying of smaller droplets cuts off electrolyte supply and accelerates stabilization.

Fig. 9f shows the average evolution of p_Y across size bins. Larger droplets stabilize at slightly higher plateau values than smaller droplets, possibly due to the influence of neighboring, actively corroding droplets. Corrosion products diffusing from adjacent droplets may accumulate in the outer ROI and compensate for the dilution effect caused by the larger areas. This diffusion-driven mechanism helps explain the stronger corrosion signal in the outer ROI of larger droplets.

These findings highlight that droplet size influences not only the likelihood but also the dynamics of corrosion, with distinct temporal behaviors observed between inner and outer regions.

4. Conclusions

This study introduced and validated a fully automated, data-driven framework for quantifying corrosion under thousands of individual droplets using time-lapse optical imaging. By converting raw image data into interpretable, probability-based metrics, the method enables a quantitative analysis of both the occurrence and kinetics of corrosion on a per-droplet basis.

Application of this framework to carbon steel revealed that corrosion behavior is strongly size-dependent, with larger droplets exhibiting a higher probability of developing significant, optically detectable corrosion. The analysis of spatial patterns distinguished two primary corrosion pathways: a 'inside-to-outside' propagation and an independent corrosion process occurring in the periphery of the droplet. Furthermore, the kinetic analysis showed that droplet size also affects the onset and rate of corrosion product formation, with distinct behaviors observed for inner versus outer regions.

By translating raw pixel data into physically meaningful metrics, this work provides a scalable platform for investigating localized corrosion kinetics and morphology in complex environments. The framework is broadly applicable to other surface processes where progression can be tracked by visual changes, which offers a powerful tool for high-throughput materials analysis.

CRediT authorship contribution statement

Arjan Mol: Writing – review & editing, Supervision, Conceptualization. **Yaiza Gonzalez-Garcia:** Writing – review & editing, Supervision, Resources, Funding acquisition, Conceptualization. **Keer Zhang:** Writing – review & editing, Writing – original draft, Methodology, Formal analysis, Data curation, Conceptualization.

Declaration of Competing Interest

The authors declare that they have no known competing financial interests or personal relationships that could have appeared to influence the work reported in this paper.

Acknowledgments

This research was carried out under Project no. T18016 in the framework of the Research Program of the Materials Innovation Institute (M2i) supported by the Dutch Government. The authors also acknowledge the use of computational resources of the DelftBlue supercomputer, provided by Delft High Performance Computing Centre (https://www.tudelft.nl/dhpc)

Appendix A. Supporting information

Supplementary data associated with this article can be found in the online version at doi:10.1016/j.corsci.2025.113313.

Data availability

The raw data is available upon request. The Python code for the analysis involved in this work is available at: https://github.com/KeerZhang345/Droplet-Optical-Microscopy-Images-Analysis

References

[1] X. Tang, C.R. Ma, X.X. Zhou, X.L. Lyu, Q. Li, Y. Li, Atmospheric corrosion local electrochemical response to a dynamic saline droplet on pure iron, Electrochem. Commun. 101 (2019) 28–34, https://doi.org/10.1016/j.elecom.2019.01.011.
[2] K. Zhang, E. Rahimi, N. van den Steen, H. Terryn, A. Mol, Y. Gonzalez-Garcia, Monitoring atmospheric corrosion under multi-droplet conditions by electrical resistance sensor measurement, DOI: ARTN 112271, Corros. Sci. 236 (2024), https://doi.org/10.1016/j.corsci.2024.112271.
[3] J. Jiang, J. Wang, Y.H. Lu, J.Z. Hu, Effect of length of gas/liquid/solid three-phase boundary zone on cathodic and corrosion behavior of metals, Electro Acta 54 (5) (2009) 1426–1435, https://doi.org/10.1016/j.electacta.2008.09.017.
[4] S.X. Li, L.H. Hihara, Atmospheric-corrosion electrochemistry of NaCl droplets on carbon steel, J. Electrochem. Soc. 159 (11) (2012) C461–C468, https://doi.org/10.1149/2.035211jes.
[5] S.X. Li, L.H. Hihara, The comparison of the corrosion of ultrapure iron and low-carbon steel under NaCl-electrolyte droplets, Corros. Sci. 108 (2016) 200–204, https://doi.org/10.1016/j.corsci.2016.03.005.
[6] B.E. Risteen, E. Schindelholz, R.G. Kelly, Marine aerosol drop size effects on the corrosion behavior of low carbon steel and high purity iron, J. Electrochem. Soc. 161 (14) (2014) C580–C586, https://doi.org/10.1149/2.1171412jes.
[7] J. Weissenrieder, C. Leygraf, Studies of filiform corrosion of iron, J. Electrochem. Soc. 151 (3) (2004) B165–B171, https://doi.org/10.1149/1.1645263.

[8] E. Schindelholz, B.E. Risteen, R.G. Kelly, Effect of relative humidity on corrosion of steel under sea salt aerosol proxies, J. Electrochem. Soc. 161 (10) (2014) C460–C470, https://doi.org/10.1149/2.0231410jes.
[9] T. Tsuru, K.I. Tamiya, A. Nishikata, Formation and growth of micro-droplets during the initial stage of atmospheric corrosion, Electro Acta 49 (17-18) (2004) 2709–2715, https://doi.org/10.1016/j.electacta.2004.01.032.
[10] N. Van den Steen, Y. Gonzalez-Garcia, J.M.C. Mol, H. Terryn, Y. Van Ingelgem, Predicting the effect of droplet geometry and size distribution on atmospheric corrosion, DOI: ARTN 110308, Corros. Sci. 202 (2022), https://doi.org/10.1016/j.corsci.2022.110308.
[11] E. Rahimi, K. Zhang, A. Kosari, N. van den Steen, A. Homborg, H. Terryn, A. Mol, Y. Gonzalez-Garcia, Atmospheric corrosion of iron under a single droplet: a new systematic multi-electrochemical approach, DOI: ARTN 112171, Corros. Sci. 235 (2024), https://doi.org/10.1016/j.corsci.2024.112171.
[12] M.Y. Wang, X.Y. Zhao, S. Gao, Y.S. Zhu, Y. Zheng, Y. Huang, Y.Z. Xu, Visualizing and understanding corrosion evolution beneath a condensed droplet using the multi-electrode array, DOI: ARTN 133252, Colloid Surf. A 684 (2024), https://doi.org/10.1016/j.colsurfa.2024.133252.
[13] N. Van den Steen, H. Simillion, O. Dolgikh, H. Terryn, J. Deconinck, An integrated modeling approach for atmospheric corrosion in presence of a varying electrolyte film, Electro Acta 187 (2016) 714–723, https://doi.org/10.1016/j.electacta.2015.11.010.
[14] I.S. Cole, T.H. Muster, N.S. Azmat, M.S. Venkatraman, A. Cook, Multiscale modelling of the corrosion of metals under atmospheric corrosion, Electro Acta 56 (4) (2011) 1856–1865, https://doi.org/10.1016/j.electacta.2010.10.025.
[15] W.C. Li, Q.L. Lian, F.F. Huang, B. Zhang, H.B. Zhang, K.N. Liu, Y.K. Jia, H.J. Wang, Y.M. Lai, Y. Jin, Numerical simulation and experimental verification on the kinetics of droplet corrosion of carbon steel, DOI: ARTN 145607, Electro Acta 514 (2025), https://doi.org/10.1016/j.electacta.2024.145607.
[16] E. Schindelholz, B.E. Risteen, R.G. Kelly, Effect of relative humidity on corrosion of steel under sea salt aerosol proxies, J. Electrochem. Soc. 161 (10) (2014) C450–C459, https://doi.org/10.1149/2.0221410jes.
[17] S. Wan, J. Hou, Z.F. Zhang, X.X. Zhang, Z.H. Dong, Monitoring of atmospheric corrosion and dewing process by interlacing copper electrode sensor, Corros. Sci. 150 (2019) 246–257, https://doi.org/10.1016/j.corsci.2019.02.008.
[18] B.G. Koushik, N. Van den Steen, M.H. Mamme, Y. Van Ingelgem, H. Terryn, Review on modelling of corrosion under droplet electrolyte for predicting atmospheric corrosion rate, J. Mater. Sci. Technol. 62 (2021) 254–267, https://doi.org/10.1016/j.jmst.2020.04.061.
[19] K.P. FitzGerald, J. Nairn, G. Skennerton, A. Atrens, Atmospheric corrosion of copper and the colour, structure and composition of natural patinas on copper, Corros. Sci. 48 (9) (2006) 2480–2509, https://doi.org/10.1016/j.corsci.2005.09.011.
[20] S. Minaee, Y.Y. Boykov, F. Porikli, A.J. Plaza, N. Kehtarnavaz, D. Terzopoulos, Image segmentation using deep learning: a survey, Ieee T Pattern Anal. 44 (7) (2022) 3523–3542, https://doi.org/10.1109/Tpami.2021.3059968.
[21] N. Otsu, Threshold selection method from gray-level histograms (Doi), Ieee T Syst. Man Cyb 9 (1) (1979) 62–66, https://doi.org/10.1109/Tsmc.1979.4310076.
[22] H. Samet, M. Tamminen, Efficient component labeling of images of arbitrary dimension represented by linear bintrees (Doi), Ieee T Pattern Anal. 10 (4) (1988) 579–586, https://doi.org/10.1109/34.3918.
[23] R. Li, A. Makogon, T. Galochkina, J.F. Lemineur, F. Kanoufi, V. Shkirskiy, Unsupervised analysis of optical imaging data for the discovery of reactivity patterns in metal alloy, Small Methods 7 (10) (2023), https://doi.org/10.1002/smtd.202300214.
[24] Wang, J.; Liu, Z.; Zhao, L.; Wu, Z.; Ma, C.; Yu, S.; Dai, H.; Yang, Q.; Liu, Y.-H.; Zhang, S.; et al. Review of Large Vision Models and Visual Prompt Engineering. *ArXiv* 2023, *abs/2307.00855*.
[25] A. Kirillov, E. Mintun, N. Ravi, H.Z. Mao, C. Rolland, L. Gustafson, T.T. Xiao, S. Whitehead, A.C. Berg, W.Y. Lo, et al., Segment anything, Ieee I Conf. Comp. Vis. (2023) 3992–4003, https://doi.org/10.1109/Iccv51070.2023.00371.
[26] G.E. Hinton, R.R. Salakhutdinov, Reducing the dimensionality of data with neural networks, Science 313 (5786) (2006) 504–507, https://doi.org/10.1126/science.1127647.
[27] P.Z. Li, Y. Pei, J.Q. Li, A comprehensive survey on design and application of autoencoder in deep learning, DOI: ARTN 110176, Appl. Soft Comput. 138 (2023), https://doi.org/10.1016/j.asoc.2023.110176.
[28] A. Savitzky, M.J.E. Golay, Smoothing + differentiation of data by simplified least squares procedures (DOI), Anal. Chem. 36 (8) (1964) 1627, https://doi.org/10.1021/ac60214a047.
[29] R.W. Schafer, What is a Savitzky-Golay filter? Ieee Signal Proc. Mag. 28 (4) (2011) 111–117, https://doi.org/10.1109/Msp.2011.941097.
[30] V. Soulié, F. Lequien, F. Ferreira-Gomes, G. Moine, D. Feron, P. Prene, H. Moehwald, T. Zemb, H. Riegler, Salt-induced iron corrosion under evaporating sessile droplets of aqueous sodium chloride solutions, Mater. Corros. 68 (9) (2017) 927–934, https://doi.org/10.1002/maco.201609319.
[31] S.P. Knight, A.D. Sudholz, A. Butler, S. Palanisamy, M.S. Dargusch, A.R. Trueman, The effect of droplet size on the localized corrosion of high-strength aluminum alloys, Mater. Corros. 67 (12) (2016) 1294–1307, https://doi.org/10.1002/maco.201609045.
[32] F. Lequien, V. Soulié, G. Moine, A. Lequien, D. Feron, P. Prene, H. Moehwald, H. Riegler, T. Zemb, Corrosion influence on the evaporation of sessile droplet, Colloid Surf. A 546 (2018) 59–66, https://doi.org/10.1016/j.colsurfa.2018.02.047.